HHS Public Access

Author manuscript

Ann Biomed Eng. Author manuscript; available in PMC 2020 August 01.

Published in final edited form as:

Ann Biomed Eng. 2019 August ; 47(8): 1786–1798. doi:10.1007/s10439-019-02285-2.

4D Flow MRI Estimation of Boundary Conditions for Patient Specific Cardiovascular Simulation

Ryan Pewowaruk[1], **Alejandro Roldán-Alzate**[1,2,3]

[1.]Biomedical Engineering, University of Wisconsin – Madison

[2.]Mechanical Engineering, University of Wisconsin – Madison

[3.]Radiology, University of Wisconsin – Madison

Abstract

Accurate image based cardiovascular simulations require patient specific boundary conditions (BCs) for inlets, outlets and vessel wall mechanical properties. While inlet BCs are typically determined non-invasively, invasive pressure catheterization is often used to determine patient specific outlet BCs and vessel wall mechanical properties. A method using 4D Flow MRI to non-invasively determine both patient specific outlet BCs and vessel wall mechanical properties is presented and results for both *in vitro* validation with a latex tube and an *in vivo* pulmonary artery stenosis (PAS) stent intervention are presented. For *in vitro* validation, acceptable agreement is found between simulation using BCs from 4D Flow MRI and benchtop measurements. For the PAS virtual intervention, simulation correctly predicts flow distribution with 9% error compared to MRI. Using 4D Flow MRI to noninvasively determine patient specific BCs increases the ability to use image based simulations as pressure catheterization is not always performed.

Keywords

Fluid Structure Interaction; 4D Flow MRI; Patient Specific; Pulmonary Artery Stenosis

Introduction

Image based computational fluid dynamics (CFD) has the capability to enhance existing diagnostic medical imaging data, investigate basic biomechanics science and inform clinical decision making[22,25,26,43] Image based CFD has been applied to numerous cardiovascular diseases including coronary artery stenosis[43], congenital heart defects[25,26,38], cerebral aneurysms[22] and aortic aneurysms[5]. Patient specific volumetric flow is typically prescribed as an inlet BC and temporally varying inlet velocity fields measured from PC-MRI are increasingly being used for increased accuracy[28,33]. Advances in numerical techniques and computational resources allow the use of patient specific vessel wall mechanical properties

1111 Highland Ave, Room 2476 WIMR 2, Madison, WI 53705 pewowaruk@wisc.edu; Phone: 507-206-1327; Web: uwcvfd.engr.wisc.edu.

in fluid-structure interaction (FSI)[7,10,23] and patient specific reduced order modeling of the distal vasculature[27,45] not immediately available from medical imaging. Using FSI with patient specific vessel mechanical properties is important for simulation accuracy as CFD simulations assuming a rigid wall have been shown to overestimate wall shear stresses and fundamentally alters the physics of pulsatile flow as waves will be propagated at infinite speed[3]. Reduced order modelling of the distal vasculature has been shown to improve velocity field accuracy compared to simply assigning outlet flow[32]. Given the importance of patient specific vessel wall[3] and distal vasculature characteristics[4,32,39] for the accuracy of model results, several studies have used pressure measurements to define these patient specific boundary conditions (BCs)[49,51,39]. In Xiao et al[49], mean pressure was used to determine distal resistance and pulse pressure to calculate distal compliance. This approach has also been combined with PC-MRI measured vascular area change over the cardiac cycle to determine vessel stiffness as shown in Figure 1A[51]. While tonometry can be used to measure pressure in the carotid, brachial and iliac arteries for estimating pressures in aortic simulations, invasive catheterization is required to measure pressure in other vascular territories such as the pulmonary or hepatic vasculature.

Our group has previously performed non-invasive MRI based virtual surgery planning in the hepatic vasculature of living donor liver transplant[41]. Moving forward we aim to further utilize MRI, particularly 4D Flow MRI, to non-invasively define patient specific BCs for computational simulations to enhance treatment planning. A particular focus is virtual planning of catheter based stent intervention for treating the congenital heart defect (CHD) pulmonary artery stenosis (PAS) in conjunction with ongoing preclinical studies in a large animal model[2] PAS is a common post-operative complication of CHD surgeries[12,14,18,31,47] and is associated with acute and chronic morbidity and mortality[9,13,36].

The goals of this paper are:

1. Present a method for defining patient specific BCs from non-invasive 4D Flow MRI
2. Validate this method using an *in vitro* model and compare simulated results to benchtop flow probe and high speed camera measurements
3. Demonstrate the feasibly of defining patient specific BCs from 4D Flow MRI *in vivo* by performing a virtual stent intervention in a porcine PAS and compare simulated results to experimental intervention outcomes

Materials and Methods

Boundary Condition Derivation

Our noninvasive method to determine patient specific BCs from 4D flow MRI is motivated by cardiovascular physics and physiology (Figure 1B). First, pulse wave velocity (PWV) is used to estimate the vessel wall stiffness (Eh, where E is elastic modulus and h is vessel wall thickness).

$$PWV^2 = \frac{Eh}{\rho_f D} \tag{1}$$

$$Eh = PWV^2 \rho_f D \tag{2}$$

PWV is calculated by taking the slope of flow versus vessel cross-sectional area curve for the initial time points of systole when there should be only forward travelling waves (Figure 2)[35]. This is derived from wave intensity analysis where flow rate (Q) and vessel cross-sectional area (A) are decomposed into forward and backwards travelling waves.

$$dQ = dQ_+ + dQ_- \tag{3}$$

$$dA = dA_+ + dA_- \tag{4}$$

It can be shown from conservation of momentum and mass equations that PWV is equal to the ratio of incremental changes in either forward or backward traveling waves.

$$PWV = \pm \frac{dQ_\pm}{dA_\pm} \tag{5}$$

The difficulty is that to decompose waves into forward and backward travelling components PWV must be known[30].

Fortunately, in early systole it is appropriate to assume that there are only forward travelling waves and thus PWV is calculated as the ratio of incremental changes in Q and A.

$$PWV \approx \left.\frac{dQ}{dA}\right|_{t\in early\ systole} \tag{6}$$

From clinical MRI images, the spatial resolution is not sufficiently high to accurately measure vessel wall thickness. Using a thin-wall assumption though, the vessel wall thickness is only present in the term Eh for vessel stiffness. By determining the total vessel stiffness from PWV vessel wall thickness and elastic modulus do not need to be independently determined.

Once stiffness is estimated from PWV, the pulse pressure (ΔP) in the vessel can be calculated from the artery area change from systole to diastole using the Law of Laplace[29].

$$\Delta P = \frac{\sigma_{\theta\theta} h}{R_{dia}} = \frac{Eh\,\varepsilon_{\theta\theta}}{R_{dia}} = \frac{Eh}{(1-\upsilon^2)R_{dia}}\left(1 - \sqrt{\frac{A_{dia}}{A_{sys}}}\right) \tag{7}$$

where $\sigma_{\theta\theta}$ is circumferential stress, R_{dia} is diastolic radius, $\epsilon_{\theta\theta}$ is circumferential strain and ν is Poisson's ratio. Distal vasculature compliance (C) can then be calculated from Q and the pulse pressure.

$$C = \frac{\Delta V}{\Delta P} = \frac{\Delta Q \, \Delta t}{\Delta P} \tag{8}$$

Lastly, an exponential decay is fit to vessel area during diastole (Fig2). The exponential time constant (τ) is assumed to be the distal vasculature time constant and used to calculate resistance. While τ for area decay will not be the same as τ for pressure decay, vessel area is a function of pressure and thus should provide an estimate of τ from which to calculate distal vasculature resistance (R).

$$P = P_1 e^{-\frac{t}{\tau}} \tag{9}$$

$$A = A_1 e^{-\frac{t}{\tau}} + A_0 \tag{10}$$

$$\tau = RC \tag{11}$$

While the values for Eh, C and R could be directly used for simulation the assumptions of circular cross-sections and straight vessel centerlines in the above derivation will likely limit accuracy. Instead, they will be used as initial guesses and over several simulation iterations Eh, C and R will be refined to decrease FSI - 4D Flow MRI error.

Boundary Condition Estimation

PWV is a function of vessel stiffness (Eq 1) but not distal resistance or compliance. Vessel stiffness is thus estimated before resistance and compliance by modulating vessel stiffness until error between measured and simulated PWV is less than 10%. Additionally, PWV is not affected by initial transients so to more rapidly estimate vessel stiffness only the initial portion of systole is simulated.

Next, full heartbeats are simulated and compliance and resistance are modulated until relative area change (RAC, $RAC = (A_{sys} - A_{dia})/A_{sys}$) and τ error is less than 10%.

An algorithmic approach[49] to varying vessel stiffness, compliance and resistance based on FSI-4D Flow MRI error was attempted. For example, vessel stiffness (Eh) was changed for FSI iteration $n+1$ based on PWV error for iteration n.

$$Eh_{n+1} = Eh_n - \rho_f D(PWV_{FSI}^2 - PWV_{MRI}^2)\,. \tag{12}$$

This approach successfully reduced FSI-4D Flow MRI error for PWV and τ below 10% but RAC error remained above 10% for many FSI iterations and was not decreasing. Parameters were instead varied in an ad hoc manner.

MRI Acquisition and Analysis

MRI data is obtained on a 3.0T imaging system using 4D Flow MRI PC-VIPR (Phase Contrast Vastly Under sampled Projection Imaging)[8,46]. Flow rates are calculated from

velocity fields using Ensight (Ansys, Canonsburg, PA). Vessel areas are calculated from time resolved velocity images using ImageJ. Flow rates and vessel areas are both measured on the same plane to calculate PWV, RAC and T. For the latex tube this plane is located at the midpoint between the inlet and outlet. For the PAS this plane is located in the MPA.

Geometry Segmentation and Mesh Generation

Geometries for FSI are segmented using the open source software Simvascular[44]. Vessel centerline points are manually placed. Vessel cross-sections are automatically segmented using a level-set method and then lofted together. Near the stenosis in the *in vivo* simulations vessel cross-sections needed to be manually delineated as the level-set method performed poorly. To simulate PAS intervention a stent is manually added to the originally segmented anatomy.

Simvascular is also used to created tetrahedral meshes for all three simulations (latex tube, PAS, PAS + stent). Mesh parameters are listed in Table 1. A mesh sensitivity study[17,34] found that the PAS mesh settings resolved wall shear stress at a location in the main pulmonary artery and within the stenosis.

FSI Implementation

FSI is performed with Simvascular[44] using a stabilized finite element method and linear shape functions for both velocity and pressure.. A coupled momentum method (CMM-FSI) approach is used for FSI[7]. We will briefly describe CMM-FSI and its assumptions, similar to the presentation of Boccadifuoco et al[3]. The differential (strong) form of the conservation of momentum equations for the vessel wall is

$$\rho_S \frac{\partial^2 \boldsymbol{d}_s}{\partial t^2} = \boldsymbol{\nabla} \cdot \boldsymbol{\sigma}_s + \boldsymbol{b}_s, \tag{13}$$

where ρ_s is the solid density, $\boldsymbol{d}_s$ is the displacement field, $\boldsymbol{\sigma}_s$ is the solid stress tensor and $\boldsymbol{b}_s$ is the volume force. By employing a thin wall approximation for the vessel wall, $\boldsymbol{b}_s$ can be represented by the vessel wall thickness h and the surface traction acting on the wall $\boldsymbol{t}_s$

$$\boldsymbol{b}_s = \frac{\boldsymbol{t}_s}{h}. \tag{14}$$

Recognizing the relationship between the traction acting on the vessel wall and the traction acting on the fluid ($\boldsymbol{t}_s = -\boldsymbol{t}_f$), the solid and fluid problems may be coupled and a unified variational formulation for the fluid - thin elastic wall problem is obtained[7]. Linear elasticity and small-displacement kinematics are assumed for the vessel wall so that the fluid domain mesh remains static[7]. This reduces the computational cost of performing FSI and is similar to the analytical solution for pulsatile flow in an elastic tube[48].

For PAS and PAS intervention simulations using realistic material properties for the Gore-Tex graft and stent prohibitively decreased the stable time-step size. The graft material in the stenosis region and the stent were instead given a stiffness two orders of magnitude greater than the vessel wall. A Poisson ratio of ½ is used for all materials.

***In Vitro*: Latex Tube—**This novel BC estimation method is applied to an *in vitro* phantom of pulsatile flow in a latex tube (Figure 3)[40]. The tube inner diameter is 15.9mm and the tube length is 130mm. The experimental fluid was water and modeled as an incompressible, Newtonian fluid with a density of $1 g/cm^3$ and a viscosity of 0.009 dyne sec cm^{-2}. The Reynold's number for this experiment is 4200.

The experimental flow loop[40] did not have distal compliance, only distal resistance so for FSI a resistance outlet BC is used. Without distal compliance the RC time constant should be zero therefore τ is not used to determine BCs, only PWV and RAC. PWV determination of initial vessel stiffness remains the same and ΔP from area change (Eq. 9) is now used to calculate initial resistance,

$$R = \frac{\Delta P}{\Delta Q} \tag{15}$$

FSI simulation results are then compared against benchtop measurements of flow and displacement for validation[40]. Flowrates measured with ultrasonic flow probes (16PXL, Transonic, NY) at the tube inlet and outlet are used to calculate benchtop PWV. PWV is calculated using a cross-correlation (XCOR) method where a cross-correlation of the flow upstroke is used to determine the inlet-to-outlet time lag. The tube length divided by the time lag gives PWV. PWV is also calculated using time-to-mid (TTM) where the 50% point of maximum flow is used to calculate inlet-to-outlet time lag. The last benchtop PWV calculation is time-to-foot (TTF) where the time axis intercept of a line fit to the flow upstroke is used to calculate inlet-to-outlet time lag. Complete details of benchtop PWV calculation may be found in Ruesink et al[40]. High-speed camera (Phantom v341, Vision Research, NJ) measurements with strain tracking (StrainMaster, LaVision, MI) were also used to calculate benchtop maximum displacement and RAC assuming a circular tube cross-section. FSI maximum displacement is the maximum wall displacement over one heartbeat.

In Vivo*: Pulmonary Artery Stenosis—In vivo* subject specific simulation of a porcine pulmonary artery stenosis (PAS) (Fig3) is performed next. Isolated left PAS was created in a neonatal piglet by suturing a short segment of 4.0mm Gore-Tex tube graft around the proximal left PA (LPA). Cardiac catheterizations with pre and post stent intervention MRI occurred at 6 weeks of age (4.5 kg). The Institutional Animal Care and Use Committee of the University of Wisconsin reviewed and approved this protocol. Blood is modeled as an incompressible - Newtonian fluid with a density of 1.06 g/cm3 and a viscosity of 0.04 dyne sec cm^{-2}. Cardiac output is 0.9 L/min and the Reynold's numbers in the MPA and the stenosis are 430 and 440 respectively.

Three-element Windkessel outlet BCs were used with a 1 to 9 ratio of proximal to distal resistance. Total resistance (R_T) and compliance (C_T) are split equally between the right and left pulmonary arteries (R/LPA) and individual outlet values are then set based on outlet area[49],

$$R^{LPA} = R^{RPA} = 2R_T;\ \frac{1}{R^i} = \left(\frac{A^i}{A_T}\right)\left(\frac{1}{2R_T}\right) \quad (15)$$

$$C^{LPA} = C^{RPA} = \frac{C_T}{2};\ C^i = \left(\frac{A^i}{A_T}\right)\left(\frac{C_T}{2}\right) \quad (16)$$

where R^{LPA}, R^{RPA}, R^i, C^{LPA}, C^{RPA}, C^i, A^i, A_T denote the total resistance of the left and right lungs, the total resistance of outlet i, the total compliance of the left and right lung, the compliance of outlet i, the area of outlet i and the total are of all right or left lung outlets.

The same vessel stiffness, compliance and resistance BCs that were estimated for the pre-intervention PAS are then applied to the anatomical model with a virtually placed stent to simulate catheter based intervention (Fig4A). The results of the virtual intervention are compared to 4D Flow MRI measurements taken immediately before and after intervention in the porcine PAS.

Results

In Vitro: Latex Tube

FSI displacements at subsequent time points show wave propagation (Figure 3A). A plot of error convergence between the FSI and 4D Flow MRI measurements for *in vitro* latex tube (Figure 3B) shows that the 10% error criterion is met by PWV at the second iteration and RAC at the third iteration. Table 2 shows the errors between validation measurements for benchtop, 4D Flow MRI and FSI. The greatest discrepancy between FSI and benchtop measurements is 52% error for TTF PWV. A prior validation study of CMM-FSI found 13% error between FSI and 2D PC-MRI[19] and reported 10% error between 2D PC-MRI and ultrasonic flow probe measurements[20]. Given that 4D Flow MRI was found to have 6-12% error compared to benchtop measurements, all FSI measurements except TTF PWV show acceptable agreement with benchtop measurements. A source of error for PWV FSI-benchtop error is that experimental flows were recorded in rigid tubing sections before and after the latex tube. The flow waveform shape will distort between rigid and flexible sections. The location of the “foot” used in the TTF PWV calculation is particularly sensitive to waveform shape and could explain why TTF PWV error is greater.

In Vivo: Pulmonary Artery Stenosis

A plot of error convergence between the FSI and 4D Flow MRI measurements for *in vivo* PAS (Figure 4B) shows that the 10% error criterion is met by PWV at the second iteration, τ at the fourth iteration and RAC at the eighth iteration. This is a comparable number of total iterations to determining BCs using pressure[49].

Virtual intervention accurately predicts post-intervention LPA flow percentage within 9% of 4D Flow MRI (Figure 5). There is larger error between FSI and 4D Flow MRI for the stenosis which could be due to difficulty segmenting an accurate stenosis geometry. Intervention is predicted to pulse pressure by 2mmHg while experimentally pulse pressure

also decreased by 2mmHg. Simulation predicts that intervention decreases vessel wall displacement and thus RAC (Figure 5). There is 20% error between FSI and 4D Flow MRI post-intervention RAC. FSI simulations over predict the intervention effectiveness for both LPA flow percentage and RAC. Virtual intervention accuracy is shown in Table 3.

Cut-planes show simulated velocity magnitude in the stenosis and stent at three time points of systole (Figure 6). Intervention decreases velocity in both the LPA and RPA and eliminates the jet impinging on the LPA wall distal to the stenosis. Simulations predict that time averaged wall shear stress (TAWSS) and oscillatory shear index (OSI) are both decreased by stent intervention (Figure 7), although TAWSS is only slightly decreased.

Discussion

Using 4D flow MRI to estimate FSI boundary conditions highlights an avenue for implementing advantages of patient specific simulation in enhancing information from medical imaging, surgery and intervention planning, and basic science research without the risks associated with catheterization. Realistically, a cardiologist will only perform invasive catheterization when necessary for treatment or diagnosis. For patient specific simulation to be widely applicable, methods for non-invasively determining BCs need to be developed and validated. This work represents a significant step towards these aims.

When performing validation against benchtop latex tube measurements, we found errors of 10%-25% between benchtop measurements and FSI for all metrics except TTF PWV (52% error). FSI-benchtop error is the compounded error of FSI-MRI and MRI-benchtop, each of which is approximately 10%. In particular, uncertainty regarding MRI flow measurements is a concern as 4D Flow MRI velocity fields will have non-trivial conservation of mass errors[37]. Error in numerical techniques should also be considered and as a rough estimate different groups have reported a 6% discrepancy[23] for the Greenshields–Weller FSI benchmark problem of flow in a deformable tube[11]. Given these various compounded errors we find the agreement of FSI and benchtop measurements to be acceptable.

We found good agreement between FSI simulation and 4D Flow MRI when virtually performing a stent intervention in a porcine PAS model. Not using realistic graft and stent material properties could cause error in our FSI simulations. However, small displacement values are seen in the stenosis and stent regions compared to the PA tissue (Figure 5C) suggesting that using a stiffness two orders of magnitude greater than the vessel wall is sufficient. FSI simulation of PAS treatment has been performed before[50]. They simulated surgical repair, not a catheter based stent intervention and used pressure catheter measurements to determine BCs. They reported 2% and 6% error for two patients between a lung perfusion scan 1-2 weeks after surgery and FSI using an adaptive outlet BC algorithm to maintain constant WSS in distal pulmonary arteries. Using pre-operative BCs they reported 23% and 18% error. Our LPA flow error was 9% between FSI and 4D Flow MRI performed immediately after intervention. Their improved accuracy using adaptive BCs for a 1-2 week post-operative measurement and our accuracy using pre-intervention BCs for an immediately post-intervention measurement suggest that the distal vasculature is adapting to the new hemodynamic conditions in that 1-2 week time frame. While the prior study and our

current study both used CMM-FSI and three element Windkessel outlets in SimVascular, the small sample sizes (n=2 and n=1) and differences in simulated treatment (surgical graft vs catheter based stent), species (human vs porcine) and clinical imaging modality (lung perfusion scan vs 4D Flow MRI) highlight that this is speculative and needs for further investigation.

This method also provides MRI quantification of distal vascular beds, which cannot be directly imaged with MRI, by calculating the distal vascular compliance, resistance and time constant from flow and area measured in the proximal vasculature. 4D Flow MRI has previously estimated proximal physiological biomarkers like pressure drop over stenosis[46], vessel stiffness through PWV[40], wall shear stress[1] and kinetic energy[15,16]. 2D PC MRI with wave intensity analysis identifies distal vascular beds properties like wave reflection sites[35] but not the more commonly used clinical markers of vascular resistance and compliance.

This method may not give as accurate of simulated pressures, particularly mean pressure, as approaches which use pressure catheterization to determine BCs. For incompressible liquids such as blood only pressure gradients drive flow not the mean pressure. For applications looking at local flow quantities such as velocity, wall shear stress or pressure gradients fitting BCs to vessel wall motion could provide more accurate results as the flow will now be solved for more accurate time resolved geometry. For other applications such as those quantifying of the effect of pathological remodeling or an intervention on ventricular afterload in a closed-loop simulation[21] simulating accurate mean pressures is important.

For CFD studies using pressure data, patient specific vessel stiffness could be determined from PWV using partial simulations (Figure 8). Resistance and compliance would then be set to match pressures. RAC could be used to validate the simulation, as it was not used in determining BC parameters. Most patient specific simulations do not validate their *in vivo* simulations against additional clinical measurements due to all clinical measurements being used to determine BCs.

A key limitation of CMM-FSI is that it solves the solid governing equations in an Eulerian reference frame so accuracy decreases with increasing deformation magnitude. This method for determining BCs could be implemented using more accurate (but more computationally expensive) numerical techniques for FSI such as arbitrary Lagrangian-Eulerian approaches or the immersed boundary method. The solid in this work was also assumed to be isotropic-linearly elastic and the unloaded geometry chosen in diastole. Determining unloaded geometries of blood vessels is an ongoing area of research[6,24] but even if the unloaded geometry could be determined a non-linear and anisotropic material model is still needed for accurate mechanical behavior[42]. Determining anisotropic properties could possibly be done from longitudinal movement of vessels measured with MRI. It is unclear how non-linear mechanical properties would be determined. Exercise or other stimuli could potentially be used to alter loading conditions. Blood vessels are relatively linear elastic in normal physiological pressure ranges so determining non-linear mechanical properties may not be necessary.

Lastly, this method could be implemented using 2D PC MRI, as these images would also provide time resolved flow rates and cross-section areas. Advantages of using a radially acquired 4D Flow MRI sequence like PC-VIPR include: no need to prospectively set planes perpendicular to flow, simultaneous acquisition of flow and anatomy, free breathing acquisition, minimization of motion artifacts and isotropic spatial resolution.

Conclusion

Flow and areas measured from 4D Flow MRI can estimate vessel wall mechanical properties and distal vasculature bed resistance and compliance for patient specific BCs. The ability to estimate BCs for patient-specific simulations without invasive catheterization increases the ability to couple FSI and 4D Flow MRI for translational and basic science studies of cardiovascular disease and eventually clinical decision making. Future work will further validate this method in additional *in vitro* phantoms as well as apply this technique to other vascular anatomies like the aorta and portal vein.

Acknowledgements

The authors would like to thank Tim Ruesink, David Rutkowski and Rafael Medero for performing the *in vitro* validation experiments and Dr. Luke Lamers for performing the *in vivo* porcine stent intervention. This investigation was supported by the National Institutes of Health, under Ruth L. Kirschstein National Research Service Award T32 HL 007936 from the National Heart Lung and Blood Institute to the University of Wisconsin-Madison Cardiovascular Research Center (RJP) and was performed using the compute resources and assistance of the UW-Madison Center For High Throughput Computing (CHTC) in the Department of Computer Sciences. The CHTC is supported by UW-Madison, the Advanced Computing Initiative, the Wisconsin Alumni Research Foundation, the Wisconsin Institutes for Discovery, and the National Science Foundation, and is an active member of the Open Science Grid, which is supported by the National Science Foundation and the U.S. Department of Energy's Office of Science.

Abbreviations

CFD	Computational Fluid Dynamics
FSI	Fluid-Structure Interaction
BC	Boundary Condition
PAS	Pulmonary Artery Stenosis
RAC	Relative Area Change
PWV	Pulse Wave Velocity
CMM-FSI	Coupled Momentum Method Fluid-Structure Interaction
XCOR	Cross Correlation
TTM	Time to Mid
TTF	Time To Foot

References

1. Barker AJ, Roldán-Alzate A, Entezari P, Shah SJ, Chesler NC, Wieben O, Markl M, and François CJ. Four-dimensional flow assessment of pulmonary artery flow and wall shear stress in adult pulmonary arterial hypertension: results from two institutions. Magn Resort Med 73:1904–1913, 2015.
2. Bates ML, Anagnostopoulos PV, Nygard C, Torgeson J, Reichert J, Galambos C, Eldridge MW, and Lamers LJ. Consequences of an early catheter-based intervention on pulmonary artery growth and right ventricular myocardial function in a pig model of pulmonary artery stenosis. Catheter Cardiovasc Interv, 2018.doi:10.1002/ccd.27593
3. Boccadifuoco A, Mariotti A, Capellini K, Celi S, and Salvetti MV. Validation of numerical simulations of thoracic aorta hemodynamics: comparison with in vivo measurements and stochastic sensitivity analysis. Cardiovasc. Eng. Technol 9: 688–706, 2018. [PubMed: 30357714]
4. Boccadifuoco A, Mariotti A, Celi S, Martini N, and Salvetti MV Impact of uncertainties in outflow boundary conditions on the predictions of hemodynamic simulations of ascending thoracic aortic aneurysms. Comput. Fluids 165:96–115, 2018.
5. Capellini K, Vignali E, Costa E, Gasparotti E, Evangelos Biancolini M, Landini L, Positano V, and Celi S. Computational Fluid Dynamic Study for aTAA Hemodynamics: An Integrated Image-Based and Radial Basis Functions Mesh Morphing Approach. J. Biomech. Eng. 140: 111007, 2018.
6. Chandra S, Gnanaruban V, Riveros F, Rodriguez JF, and Finol EA. A Methodology for the Derivation of Unloaded Abdominal Aortic Aneurysm Geometry With Experimental Validation. J Biomech Eng 138: 101005, 2016.
7. Figueroa CA, Vignon-Clemental IE, Jansen KE, Hughes TJR, and Taylor CA. A coupled momentum method for modeling blood flow in three-dimensional deformable arteries. Comput. Methods Appl Mech. Eng. 195:5685–5706, 2006.
8. François CJ, Srinivasan S, Schiebler ML, Reeder SB, Niespodzany E, Landgraf BR, Wieben O, and Frydrychowicz A. 4D cardiovascular magnetic resonance velocity mapping of alterations of right heart flow patterns and main pulmonary artery hemodynamics in tetralogy of Fallot. J Cardiovasc Magn Reson 14:16, 2012. [PubMed: 22313680]
9. Gatzoulis MA, Balaji S, Webber SA, Siu SC, Hokanson JS, Poile C, Rosenthal M, Nakazawa M, Moller JH, Gillette PC, Webb GD, and Redington AN. Risk factors for arrhythmia and sudden cardiac death late after repair of tetralogy of Fallot: a multicentre study. Lancet 356:975–981, 2000. [PubMed: 11041398]
10. Gilmanov A, and Sotiropoulos F. A hybrid Cartesian/immersed boundary method for simulating flows with 3D, geometrically complex, moving bodies. J. Comput. Phys. 207:457–492, 2005.
11. Greenshields CJ, and A WHG unified formulation for continuum mechanics applied to fluid-structure interaction in flexible tubes. Int. J. Numer. Methods Eng. 64:1575–1593, 2005.
12. Groh MA, Meliones JN, Bove EL, Kirklin JW, Blackstone EH, Lupinetti FM, Snider AR, and Rosenthal A. Repair of tetralogy of Fallot in infancy. Effect of pulmonary artery size on outcome. Circulation 84:III206–12, 1991. [PubMed: 1934412]
13. Harrison DA, Harris L, Siu SC, MacLoghlin CJ, Connelly MS, Webb GD, Downar E, McLaughlin PR, and Williams WG. Sustained ventricular tachycardia in adult patients late after repair of tetralogy of Fallot. J Am Coll Cardiol 30:1368–1373, 1997. [PubMed: 9350941]
14. Hirsch JC, Mosca RS, and Bove EL. Complete repair of tetralogy of Fallot in the neonate: results in the modern era. Ann Surg 232:508–514, 2000. [PubMed: 10998649]
15. Hussaini SF, Rutkowski DR, Roldán-Alzate A, and François CJ. Left and right ventricular kinetic energy using time-resolved versus time-average ventricular volumes. J Magn Reson Imaging 45:821–828, 2017. [PubMed: 27504591]
16. Jeong D, Anagnostopoulos PV, Roldan-Alzate A, Srinivasan S, Schiebler ML, Wieben O, and François CJ. Ventricular kinetic energy may provide a novel noninvasive way to assess ventricular performance in patients with repaired tetralogy of Fallot. J Thorac Cardiovasc Surg 149:1339–1347, 2015. [PubMed: 25623907]

17. Kheyfets VO, O'Dell W Smith T Reilly JJ and Finol EA Considerations for numerical modeling of the pulmonary circulation--a review with a focus on pulmonary hypertension. J Biomech Eng 135:61011–61015, 2013. [PubMed: 23699723]
18. Kim H, Sung SC, Chang YH, Lee HD, and Park JA. Early and midterm outcomes of left pulmonary artery angioplasty using an anterior wall flap of the main pulmonary artery in tetralogy of Fallot repair. J Thorac Cardiovasc Surg 148:2597–2601, 2014. [PubMed: 24332114]
19. Kung EO, Les AS, Figueroa CA, Medina F, Arcaute K, Wicker RB, McConnell MV, and Taylor CA. In vitro validation of finite element analysis of blood flow in deformable models. Ann Biomed Eng 39:1947–1960, 2011. [PubMed: 21404126]
20. Kung EO, Les AS, Medina F, Wicker RB, McConnell MV, and Taylor CA. In vitro validation of finite-element model of AAA hemodynamics incorporating realistic outlet boundary conditions. J Biomech Eng 133:41003, 2011.
21. Kung E, Pennati G, Migliavacca F, Hsia TY, Figliola R, Marsden A, Giardini A, and Investigators M. A simulation protocol for exercise physiology in Fontan patients using a closed loop lumped-parameter model. J Biomech Eng 136: 081007, 2014.
22. Liang L, Steinman DA, Brina O, Chnafa C, Cancelliere NM, and Pereira VM. Towards the Clinical utility of CFD for assessment of intracranial aneurysm rupture - a systematic review and novel parameter-ranking tool. J Neurointerv Surg, 2018.doi: 10.1136/neurintsurg-2018-014246
23. Liu J, and Marsden AL. A unified continuum and variational multiscale formulation for fluids, solids, and fluid-structure interaction. Comput Methods Appl Mech Eng 337:549–597, 2018. [PubMed: 30505038]
24. Lu J, Zhou X, and Raghavan ML. Inverse elastostatic stress analysis in pre-deformed biological structures: Demonstration using abdominal aortic aneurysms. J. Biomech. 40:693–696, 2007. [PubMed: 16542663]
25. Marsden AL, and Esmaily-Moghadam M. Multiscale Modeling of Cardiovascular Flows for Clinical Decision Support. Appl. Mech. Rev. 67:11, 2015.
26. Marsden AL, and Feinstein JA. Computational modeling and engineering in pediatric and congenital heart disease. Curr Opin Pediatr 27:587–596, 2015. [PubMed: 26262579]
27. Moghadam ME, Bazilevs Y, Hsia T-Y, Vignon-Clemental IE, and Marsden AL. A comparison of outlet boundary treatments for prevention of backflow divergence with relevance to blood flow simulations. Comput. Mech. 48:277–291, 2011.
28. Morbiducci U, Ponzini R, Gallo D, Bignardi C, and Rizzo G. Inflow boundary conditions for image-based computational hemodynamics: Impact of idealized versus measured velocity profiles in the human aorta. J. Biomech. 46:102–109, 2012. [PubMed: 23159094]
29. Olufsen MS Structured tree outflow condition for blood flow in larger systemic arteries. Am. J. Physiol. Hear. Circ. Physiol. 276:H257–H268, 1999.
30. Parker KH An introduction to wave intensity analysis. Med Biol Eng Comput 47:175–188, 2009. [PubMed: 19205773]
31. Parry AJ, McElhinney DB, Kung GC, Reddy VM, Brook MM, and Hanley FL. Elective primary repair of acyanotic tetralogy of Fallot in early infancy: overall outcome and impact on the pulmonary valve. J Am Coll Cardiol 36:2279–2283, 2000. [PubMed: 11127473]
32. Pirola S, Cheng Z, Jarral OA, O'Regan DP, Pepper JR, Athanasiou T, and Xu XY. On the choice of outlet boundary conditions for patient-specific analysis of aortic flow using computational fluid dynamics. J Biomech 60:15–21, 2017. [PubMed: 28673664]
33. Pirola S, Jarral o. A., O'regan DP, Asimakopoulos G, Anderson JR, Pepper JR, Athanasiou T, and Xu XY. Computational study of aortic hemodynamics for patients with an abnormal aortic valve: The importance of secondary flow at the ascending aorta inlet ARTICLES YOU MAY BE INTERESTED IN Computational study of aortic hemodynamics for patients with an abnormal aortic valve: The importance of secondary flow at the ascending aorta inlet. APL Bioeng 2:26101, 2018.
34. Prakash S, and Ethier CR. Requirements for mesh resolution in 3D computational hemodynamics. J Biomech Eng 123:134–144, 2001. [PubMed: 11340874]

35. Quail MA, Knight DS, Steeden JA, Taelman L, Moledina S, Taylor AM, Segers P, Coghlan GJ, and Muthurangu V. Noninvasive pulmonary artery wave intensity analysis in pulmonary hypertension. Am J Physiol Hear. Circ Physiol 308:H1603–11, 2015.
36. Rhodes J, Dave A, Pulling MC, Geggel RL, Marx GR, Fulton DR, and Hijazi ZM. Effect of pulmonary artery stenoses on the cardiopulmonary response to exercise following repair of tetralogy of Fallot. Am J Cardiol 81:1217–1219, 1998. [PubMed: 9604951]
37. Roldán-Alzate A, Frydrychowicz A, Niespodzany E, Landgraf BR, Johnson KM, Wieben O, Reeder SB, and Roldán-Alzate A. In vivo Validation of 4D Flow MRI for Assessing the Hemodynamics of Portal Hypertension. J Magn Reson Imaging 37:1100–1108, 2013. [PubMed: 23148034]
38. Roldán-Alzate A, García-Rodríguez S, Anagnostopoulos PV, Srinivasan S, Wieben O, and François CJ. Hemodynamic study of TCPC using in vivo and in vitro 4D Flow MRI and numerical simulation. J Biomech 48:1325–1330, 2015. [PubMed: 25841292]
39. Romarowski RM, Lefieux A, Morganti S, Veneziani A, and Auricchio F. Patient-specific CFD modelling in the thoracic aorta with PC-MRI-based boundary conditions: A least-square three-element Windkessel approach., 2018.doi:10.1002/cnm.3134
40. Ruesink T, Medero R, Rutkowski D, and Roldán-Alzate A. In Vitro Validation of 4D Flow MRI for Local Pulse Wave Velocity Estimation. Cardiovasc Eng Technol, 2018.doi: 10.1007/s13239-018-00377-z
41. Rutkowski DR, Reeder SB, Fernandez LA, and Roldán-Alzate A. Surgical planning for living donor liver transplant using 4D flow MRI, computational fluid dynamics and in vitro experiments. Comput Methods Biomech Biomed Eng Imaging Vis 6:545–555, 2018. [PubMed: 30094106]
42. Sacks MS, and Sun W. Multiaxial Mechanical Behavior of Biological Materials. Annu. Rev. Biomed. Eng. 5:251–284, 2003. [PubMed: 12730082]
43. Taylor CA, Fonte TA, and Min JK. Computational fluid dynamics applied to cardiac computed tomography for noninvasive quantification of fractional flow reserve: scientific basis. J Am Coll Cardiol 61:2233–2241, 2013. [PubMed: 23562923]
44. Updegrove A, Wilson NM, Merkow J, Lan H, Marsden AL, and Shadden SC. SimVascular: An Open Source Pipeline for Cardiovascular Simulation. Ann. Biomed. Eng. 45:525–541, 2017. [PubMed: 27933407]
45. Vignon-Clemental IA, Figueroa CA, Jansen KE, and Taylor CA. Outflow boundary conditions for 3D simulations of non-periodic blood flow and pressure fields in deformable arteries. Comput. Methods Biomech. Biomed. Eng. 13:625–640, 2010.
46. Wieben O, Francois C, and Reeder SB. Cardiac MRI of ischemic heart disease at 3 T: Potential and challenges. Eur. J. Radiol. 65:15–28, 2008. [PubMed: 18077119]
47. Wilder TJ, Van Arsdell GS, Pham-Hung E, Gritti M, Hussain S, Caldarone CA, Redington A, and Hickey EJ. Aggressive Patch Augmentation May Reduce Growth Potential of Hypoplastic Branch Pulmonary Arteries After Tetralogy of Fallot Repair. Ann Thorac Surg 101:996–1004, 2016. [PubMed: 26830224]
48. Womersley JR Oscillatory motion of a viscous liquid in a thin walled elastic tube - I: the linear approximation for long waves. Philos. Mag. 7:199–221, 1955.
49. Xiao N, Alastruey J, and Alberto Figueroa C. A systematic comparison between 1-D and 3-D hemodynamics in compliant arterial models. Int J Numer Method Biomed Eng 30:204–231,2014. [PubMed: 24115509]
50. Yang W, Feinstein J, and Vignon-Clementel IE. Adaptive outflow boundary conditions improve post-operative predictions after repair of peripheral pulmonary artery stenosis. Biomech. Model. Mechanobiol. 15:1345–1353, 2016. [PubMed: 26843118]
51. Zambrano BA, McLean NA, Zhao X, Tan JL, Zhong L, Figueroa CA, Lee LC, and Baek S. Image-based computational assessment of vascular wall mechanics and hemodynamics in pulmonary arterial hypertension patients. J Biomech 68:84–92, 2018. [PubMed: 29310945]

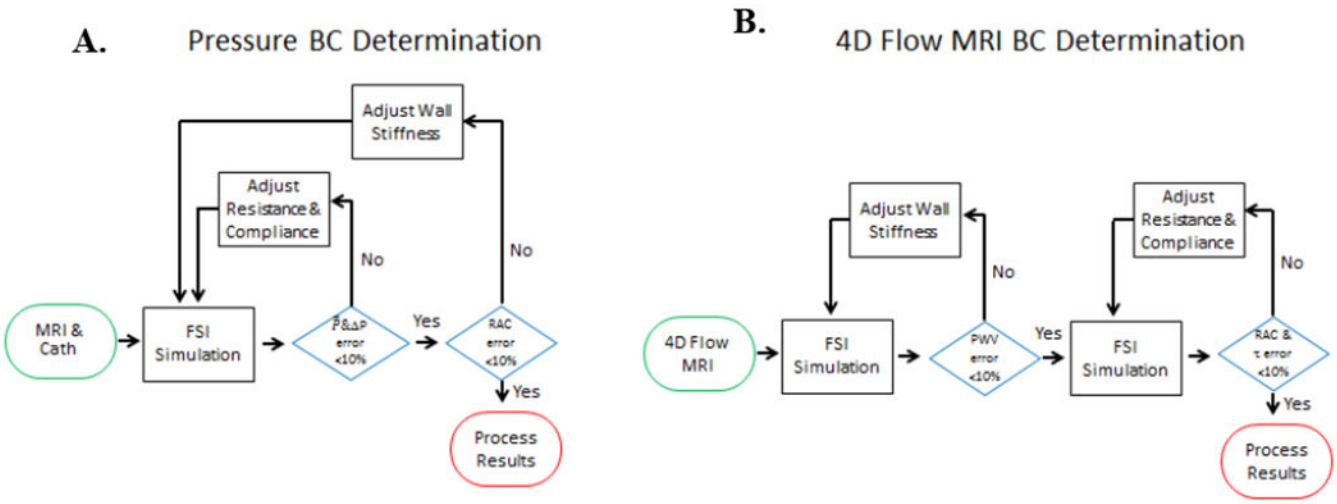

Figure 1:

A. Flow chart describing the algorithm to determine patient specific conditions from pressure. An internal loop is used to match pressure data, then an external loop modulates vessel stiffness to match RAC. Every time vessel stiffness is changed resistance and compliance must be re-fit. **B.** Flow chart describing the algorithm to determine patient specific conditions from 4D Flow MRI. An initial iterative loop is used to rapidly match PWV and then a second loop matches RAC and T.

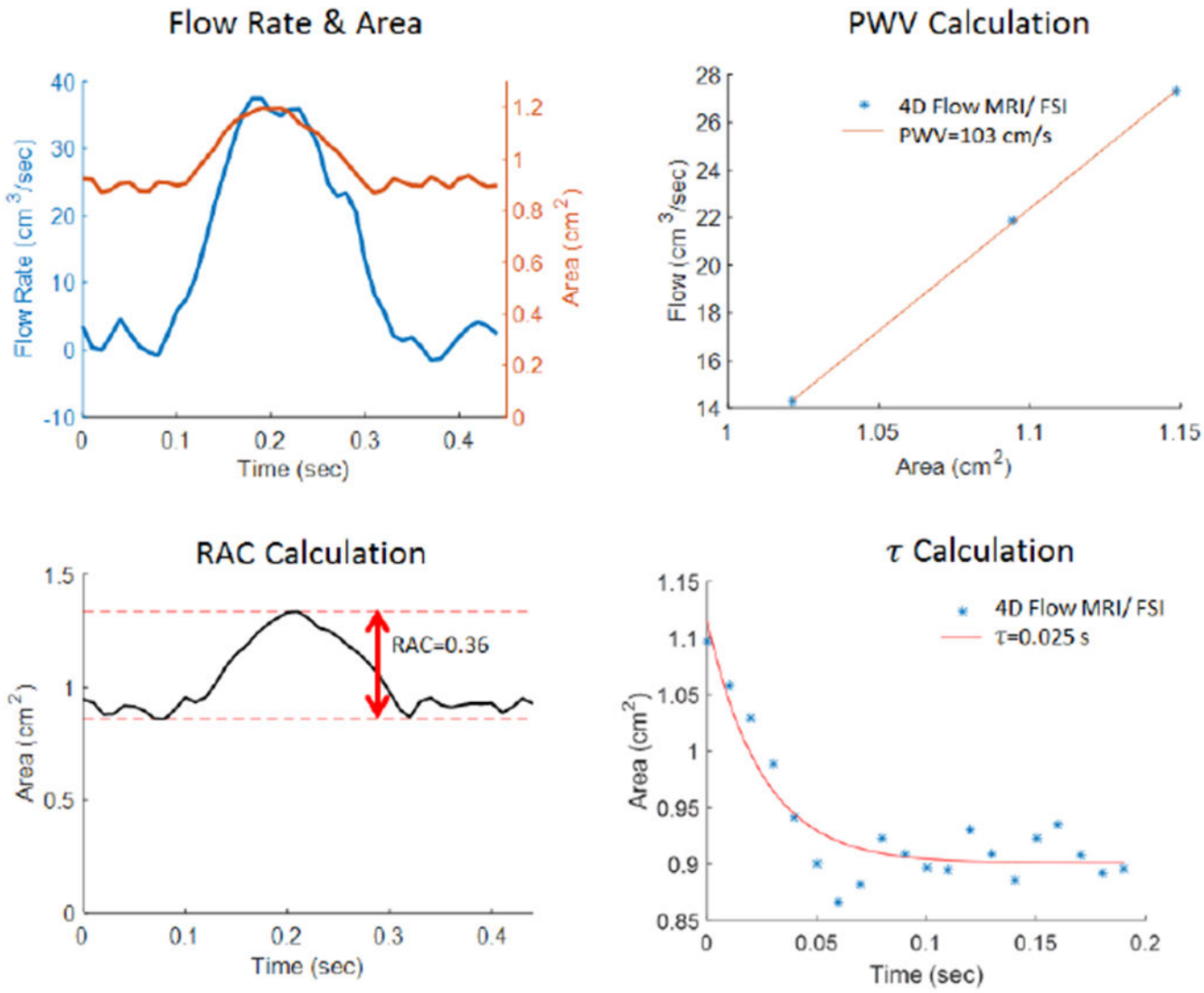

Figure 2:

Plots showing how flow rate and vessel cross-sectional area are used in the calculation of PWV, RAC and T.

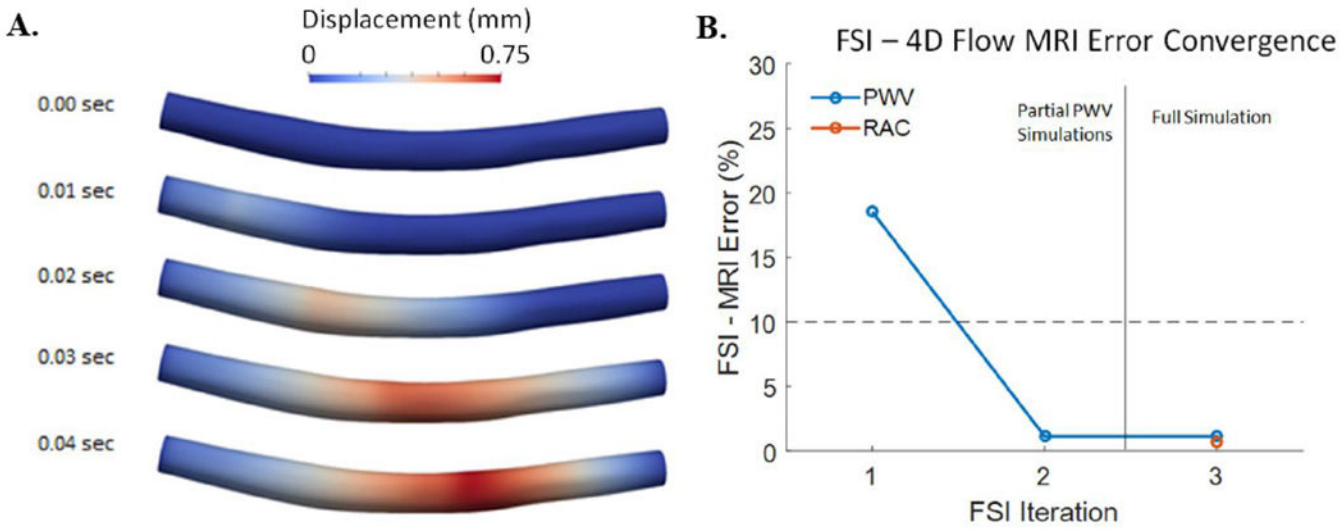

Figure 3:

A. Simulated latex tube displacements show wave propagation from the inlet (left) to outlet (right). The tube geometry is curved downwards due to gravity. **B.** FSI-4D Flow MRI error plots of the *in vitro* latex tube showing the convergence of PWV and RAC over the course of 3 FSI simulation iterations.

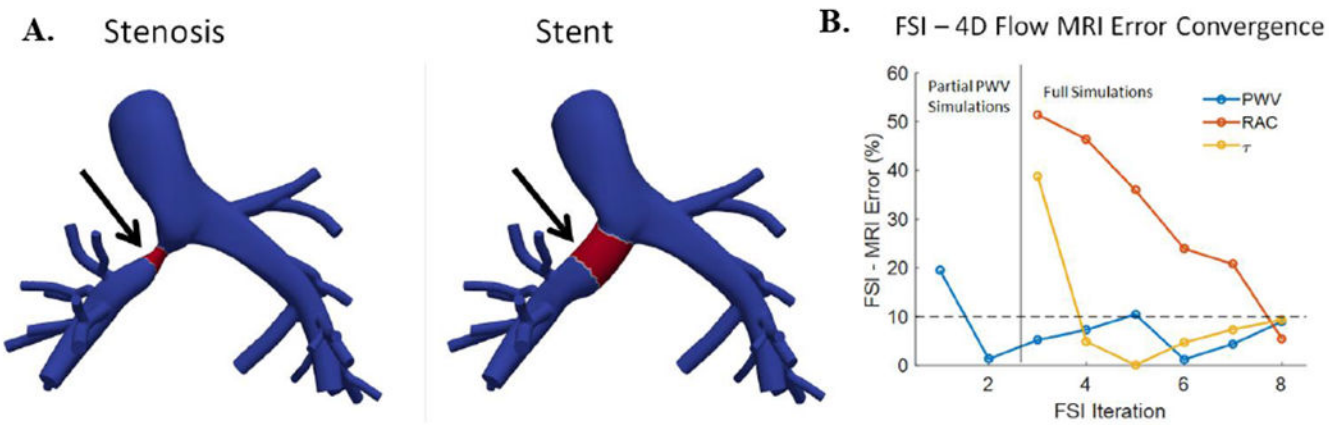

Figure 4:

A. PAS stenosis geometry and stented geometry. Black arrows point to regions where the stiffness was increased (colored red) to represent the Gore-Tex graft (stenosis) and stent. **B.** FSI-4D Flow MRI error plots of the *in vitro* latex tube showing the convergence of PWV and RAC over the course of 8 FSI simulation iterations.

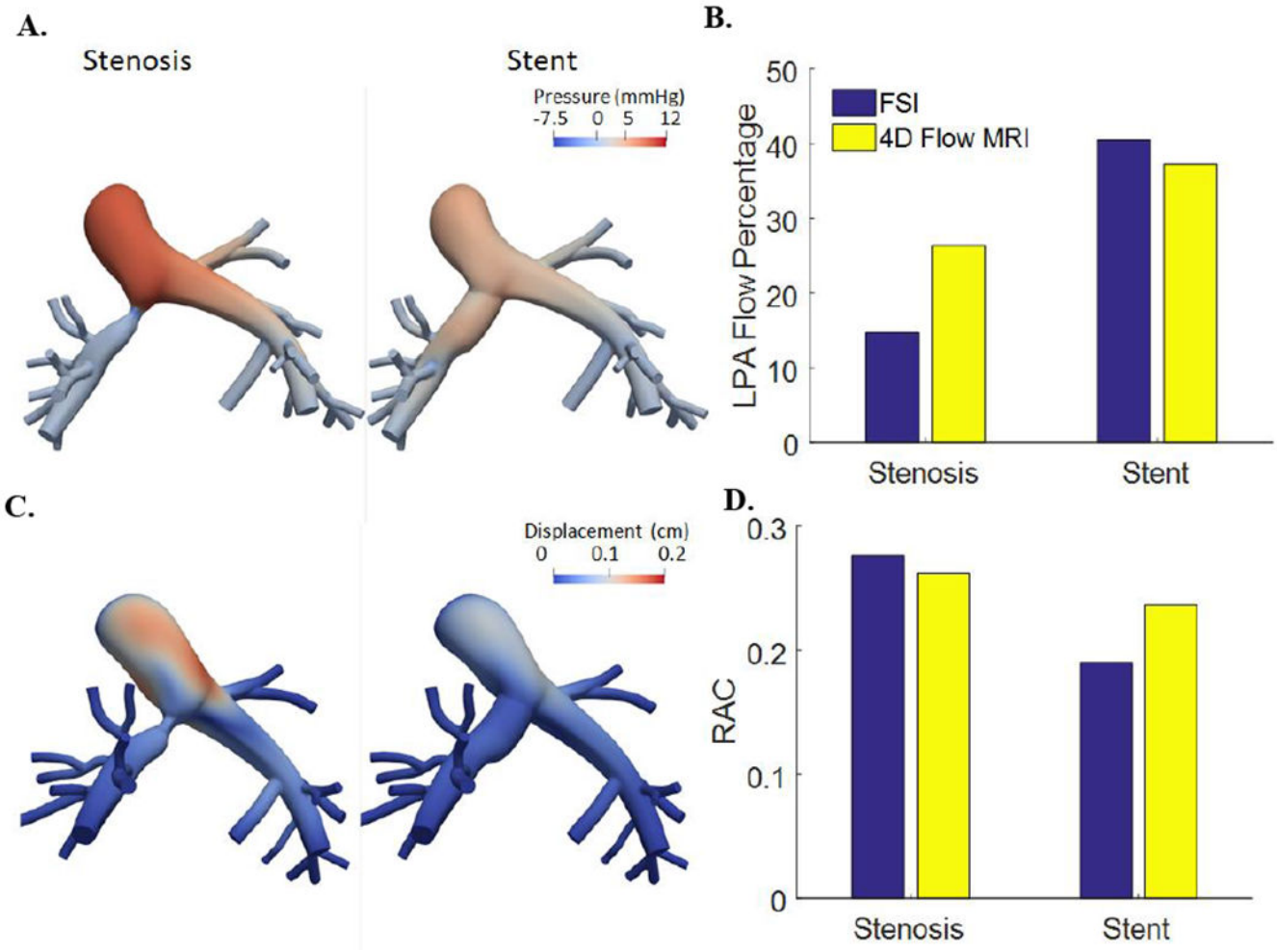

Figure 5:

Virtual intervention **A.** predicts that pressure is decreased, **B**. predicts increased LPA flow percentage with 9% accuracy, **C**. predicts decreased vessel wall displacement, and **D**. predicts decreased RAC with 20% accuracy.

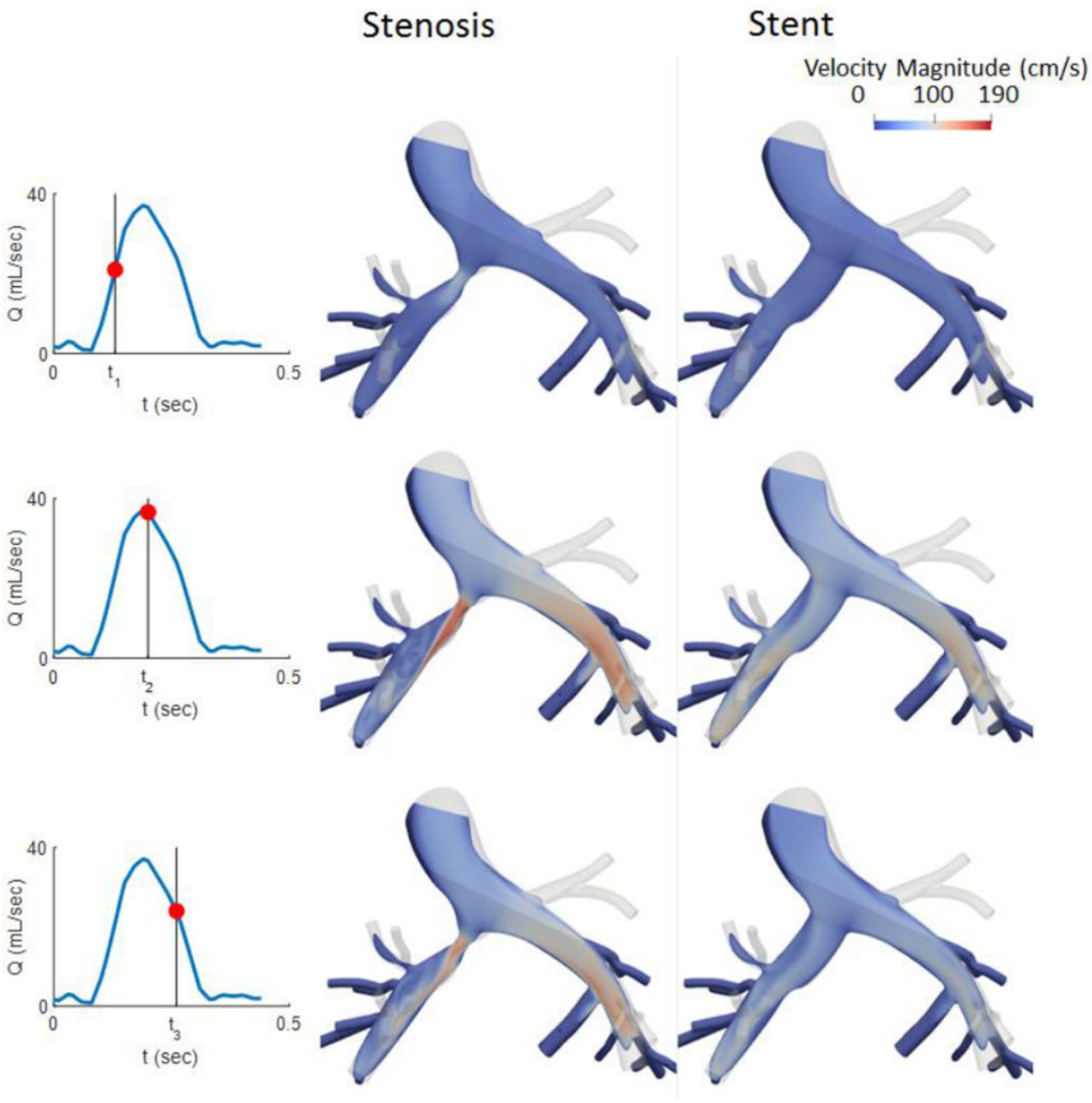

Figure 6:
FSI velocity magnitude is shown on cut planes in MPA, LPA and RPA for time points in early, peak and late systole. The 3D geometry is shown as transparent. A jet is seen impinging on the LPA wall distal to the stenosis which stent intervention is predicted to eliminate.

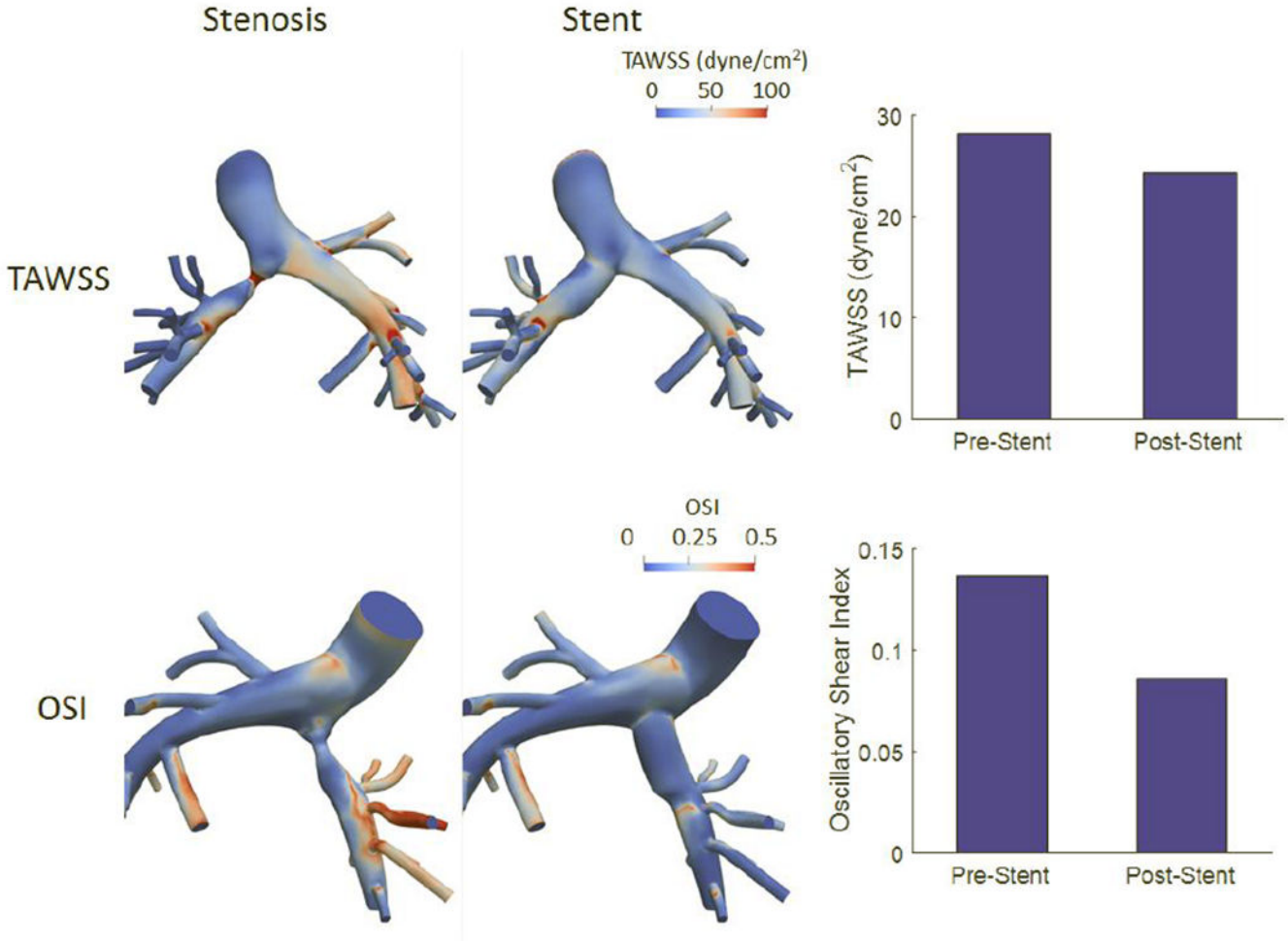

Figure 7:
FSI TAWSS and OSI are shown before and after intervention. Stent intervention is predicted to decrease both TAWSS and OSI.

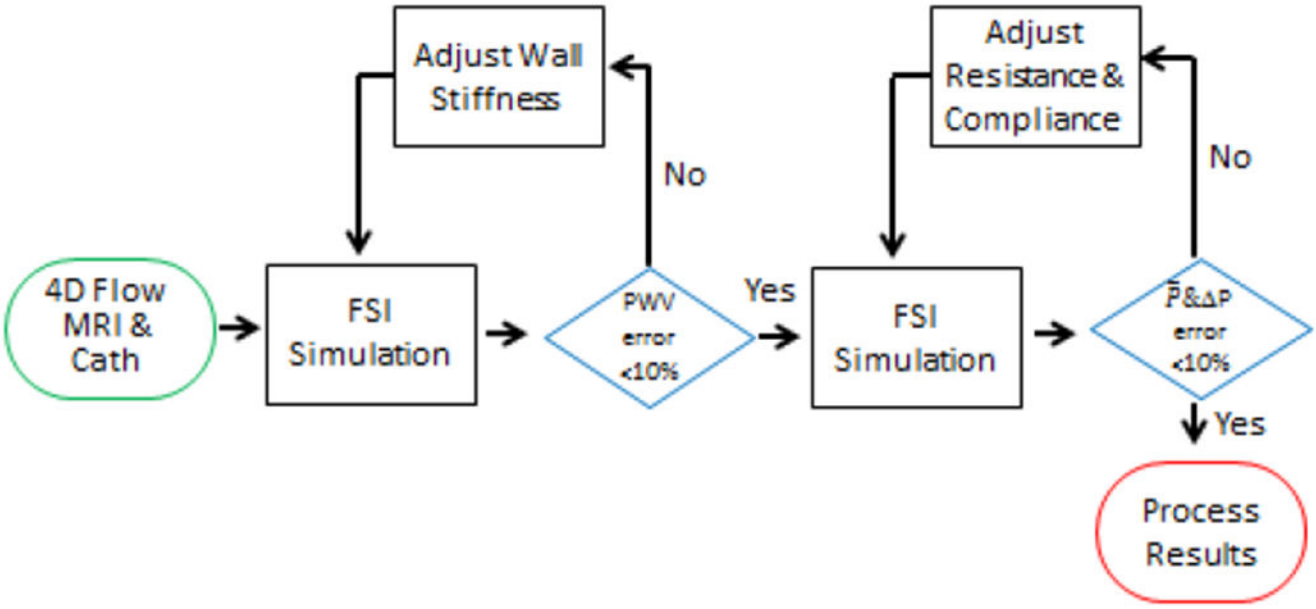

Figure 8:

Flow chart describing an algorithm to determine patient specific conditions from PWV and pressure measurements. An initial iterative loop is used to rapidly match PWV, then a second loop matches pressures. RAC would then remain as a validation measurement as it was not used to determine BCs.

Table 1:

Mesh Parameter

Geometry	Max Edge Size (mm)	Boundary Layers	Element #
Latex Tube	1.5	2	200k
PAS *	0.5	4	1M
PAS + Stent	0.5	4	1M

* The PAS mesh is refined to a 0.3mm max edge size near the stenosis

Table 2:

FSI Validation Against Benchtop Measurements

Measurement	Benchtop[40]	MRI[40]	FSI	MRI Error	FSI Error
XCOR PWV (cm/sec)	110 ± 3	103	83	6%	25%
TTM PWV (cm/sec)	93 ±2	86	102	7%	10%
TTF PWV (cm/sec)	126 ±6	134	192	7%	52%
RAC *	0.32 ± 0.003	0.28	0.28	12%	12%
Max Displacement (mm)	1.73 ± 0.02	--	1.98	--	15%

* FSI wall mechanical properties and distal resistance were tuned to match RAC from MRI

Table 3:

Virtual Intervention Accuracy

Measurement	Experiment	FSI	Error
LPA Flow Percentage	37%	40%	9%
RAC	0.24	0.19	20%